Retention of water in subducted slabs under core-mantle boundary conditions

Yutaro Tsutsumi[1]*, Naoya Sakamoto[2], Kei Hirose[1,3]*, Shoh Tagawa[1,3], Koichiro Umemoto[3], Yasuo Ohishi[4] & Hisayoshi Yurimoto[2,5]

[1]Department of Earth and Planetary Science, The University of Tokyo, Bunkyo, Tokyo, Japan.

[2]Creative Research Institution (CRIS), Hokkaido University, Sapporo, Hokkaido, Japan.

[3]Earth-Life Science Institute, Tokyo Institute of Technology, Meguro, Tokyo, Japan.

[4]Japan Synchrotron Radiation Research Institute, SPring-8, Sayo, Hyogo, Japan.

[5]Department of Natural History Sciences, Hokkaido University, Sapporo, Hokkaido, Japan.

*e-mail: tsutsumi-yutaro988@g.ecc.u-tokyo.ac.jp; kei@elsi.jp

The hydrated SiO_2 phase is a main carrier of water in subducting slabs in the lower mantle. Assuming its dehydration under high temperatures above the core-mantle boundary, it has been speculated that seismic anomalies observed in this enigmatic region and the uppermost core might be attributable to water released from slabs. Here we report melting experiments on a hydrous basalt up to conditions of the core-mantle boundary region at 25–144 gigapascals and 2,900–4,100 kelvin. Secondary ion mass spectrometry measurements with high-resolution imaging techniques reveal that the SiO_2 phase and SiO_2-AlOOH solid solution contain 0.5–3.6 wt% and ~3.5 wt% H_2O, respectively, coexisting with melts holding 0.9–2.6 wt% H_2O. The

large solubility into SiO_2 and high SiO_2/melt partition coefficient of water under high temperatures of the core-mantle boundary region suggest that practically water does not escape from subducted slabs at the base of the mantle. Even if the core-mantle boundary temperature is high enough to melt subducted crustal materials, most of the H_2O would remain in the solid residue rather than entering a partial melt. Previously proposed consequences of slab dehydration are therefore unlikely to be responsible for chemical heterogeneities in the lowermost mantle and the topmost core.

The carriers of water in cold subducting slabs (former oceanic lithosphere) have been explored by experiments and theory at high pressures[1,2]. While the slab's crustal layer may almost completely dehydrate at shallower than ~300 km depth[3], the hydrated slab mantle[4,5] can transport H_2O by hydrous phases down to the uppermost lower mantle (~700 km depth) or at most to the mid-lower mantle (~1,500 km depth)[6–9] depending on slab temperatures (see red stars in Fig. 1)[1,2]. Beyond these depths, part of the released water will dissolve into surrounding, nominally anhydrous minerals of bridgmanite and ferropericlase in the depleted peridotite layer of the slab, whose water capacity has been reported to be <0.01 wt%[10,11] to 0.1 wt% level[12,13]. It will also migrate into an overlying crustal layer of the slab and hydrate the dense SiO_2 phase[2,14–18] in particular, which is a

major constituent of subducting crustal materials[19–22]. Recent experiments performed along the cold to normal lower-mantle geotherm (Fig. 1) demonstrated that SiO_2 can hold up to ~3.5[17,18] or ~10 wt% H_2O[15,16]. It suggests that the hydrated SiO_2 phase, rather than AlOOH-$Mg_{0.5}Si_{0.5}$OOH-FeOOH solid solution (ss.)[1,23–25], is likely to be a primary host for water in the slab at greater depths (>700–1,500 km) to the bottom of the mantle[2,14–17].

Regardless of the high capacity of water in dense SiO_2, it has been speculated[1,2] and recently demonstrated by experiments on the SiO_2-H_2O system[17] that the subducted slabs will dehydrate under high temperatures in the core-mantle boundary (CMB) region. The temperature at the CMB has been estimated to be 3,400 K[26,27] to ~4,000 K[28,29] considering the solidus temperature of a pyrolitic lowermost mantle or 3,470–3,880 K based on seismic shear velocity and attenuation[30]. The released water will give rise to chemical heterogeneities indicated by seismological observations. Water can induce melting and melt migration, and hydration of lowermost mantle materials which might create the large low shear velocity provinces (LLSVPs)[1,31]. Furthermore, the reaction of water with core metal may form superoxidized $FeOOH_x$ ($x<1$)[32–34] that could account for the ultralow velocity zones (ULVZs)[35]. Also, it might develop a low-velocity layer in the topmost core[36,37].

Nevertheless, the solubility and partitioning of water into Al-bearing hydrous SiO_2 included in subducted former crustal rocks, especially mid-oceanic ridge basalt (MORB), have not been examined at high pressures and temperatures (*P*-*T*) of the CMB region, and therefore the dehydration of subducted slabs and their consequences have not been verified yet.

Water in Al-bearing SiO_2 at CMB

We have conducted 19 separate melting experiments on a hydrous MORB up to the lowermost mantle pressure range and 4,100 K in a laser-heated diamond-anvil cell (Fig. 1 and Table 1, see Methods). Melting textures and chemical compositions including the H_2O contents in melt and coexisting solids were examined on recovered samples (Fig. 2). They exhibit a concentric texture; a round pocket of quenched partial melt at the center, surrounded by the SiO_2 phase, $CaSiO_3$ perovskite (davemaoite), SiO_2-AlOOH ss.[7] and bridgmanite at 25–59 GPa (Fig. 2a). At 100 GPa and above, SiO_2 was still present next to a melt pool, and bridgmanite/post-perovskite appeared closer to melt than at lower pressures (Fig. 2b). Such zonation represents the sequence of crystallization with decreasing temperature[38,39] and is different from that of an anhydrous MORB material[40,41] because of the addition of water and the lesser amount of CaO in the present sample. Synchrotron X-ray diffraction (XRD) patterns of these samples indicate that $CaCl_2$-type

SiO_2 appeared down to at least 25 GPa at 2,900 K (22 GPa at 300 K), consistent with earlier experimental[42] and theoretical[43] findings that $CaCl_2$-type SiO_2 is stabilized with respect to stishovite in the presence of Al_2O_3 and H_2O, while it forms above 65–75 GPa at ~1,500–2,000 K in Al-free, dry SiO_2[44] and SiO_2-H_2O systems[17]. They also show a change in the crystal structure of SiO_2 from $CaCl_2$-type to α-PbO_2-type (seifertite)[19] above 128 GPa in the lowermost mantle (Fig. 1). The coexistence of SiO_2 and SiO_2-AlOOH ss. phases (Fig. 2a and Extended Data Fig. 1) suggests a miscibility gap in the SiO_2–AlOOH system as predicted by earlier theoretical calculations[7].

Water concentrations in the SiO_2 phase, SiO_2-AlOOH ss. and partial melts were determined by secondary ion mass spectrometry (SIMS) coupled with high-resolution imaging techniques (Fig. 2 and Extended Data Fig. 2) (see Methods), while in earlier studies the H_2O content in SiO_2 was estimated from Fourier-transform infrared absorption spectra[14,18], or volume expansion based on their relationship that was observed at 1 bar[15,16] or theoretically calculated at high pressures[17]. The present SIMS analyses show the hydrogen (water) abundances with ±1 to 10% fractional uncertainty; i) 0.5–3.6 wt% and 1.7–2.2 wt% H_2O in hydrated SiO_2 with the $CaCl_2$- and α-PbO_2-type structures, respectively, ii) 3.4–3.5 wt% H_2O in SiO_2-AlOOH ss. and iii) 0.9–2.6 wt% H_2O in partial melts (Table 1).

The water content in Al-bearing $CaCl_2$-type SiO_2 substantially increased with increasing pressure to 3.6 wt% H_2O at 121 GPa under 3,450 K (Figs. 3a, b). It is much higher than the recent H_2O solubility estimate of only 0.4 wt% at this *P*-*T* condition based on experiments on the Al-free SiO_2-H_2O system[17]. Such contradiction suggests that the charge-coupled substitution $Si^{4+} = Al^{3+} + H^+$ is a key mechanism for water incorporation into Al-bearing $CaCl_2$-[18] and α-PbO_2-type SiO_2 (Fig. 3c), in contrast to interstitial incorporation of molecular H_2O into Al-free SiO_2[17]. Our XRD study finds that the magnitude of orthorhombic distortion was enhanced with increasing pressure (Fig. 3d) and such crystallographic distortion correlates strongly with its water content (Fig. 3e). The enhanced distortion shortens the distance between specific pairs of oxygen atoms, making hydrogen bonds stronger and stabilizing hydrogen in SiO_2[43,45]. Moreover, previous molecular dynamics simulations[43] of hydrated SiO_2 showed superionic proton motion at 60 GPa and >1,300 K, hopping around possible sites with diffusion along the *c*-axis. Such superionic proton motion could lead to the entropic stabilization of the hydrated SiO_2 phase to high temperatures. The overall increase in water concentration in $CaCl_2$-type SiO_2 with increasing pressure results in an increase in the partition coefficient of water, D_{H2O} ($CaCl_2$-SiO_2/melt) from ~0.2 at 25 GPa to 1.4 under deep lower-mantle conditions above 120 GPa (Fig. 3f).

The H_2O contents in Al-bearing α-PbO_2-type SiO_2 formed at 3,650–4,100 K and 128–144 GPa, corresponding to conditions of the Earth's CMB region, were almost constant at 2 wt% (Fig. 3a). They are substantially higher than recently reported in the SiO_2-H_2O system (0.3–1.0 wt% H_2O)[17] at 2,820–4,100 K and 142–152 GPa, likely because of the $Si^{4+} = Al^{3+} + H^+$ charge-coupled substitution in α-PbO_2-type SiO_2 as well (Fig. 3c). D_{H2O} (α-PbO_2-SiO_2/melt) ranged from 1.1 to 2.1 (Fig. 3f), indicating that water is partitioned into hydrated SiO_2 more than into coexisting partial melts under CMB conditions. The nearly constant ~2 wt% H_2O in α-PbO_2-type SiO_2 found in all of six separate runs, while water concentrations in coexisting melts varied by a factor of two, might suggest that ~2 wt% is the maximum solubility of water and D_{H2O} (α-PbO_2-SiO_2/melt) could be higher when the SiO_2 phase is not saturated with water. While it was not found in our melting experiments, hydrous Al-rich hexagonal niccolite (hNT)-type SiO_2[16] was previously reported above 84 GPa[46]. It is similar in composition to $CaCl_2$-structured SiO_2-AlOOH ss. observed in this study and might appear in a hydrated MORB material coexisting with α-PbO_2-type SiO_2 under high *P*-*T* conditions of the CMB region.

Escape of Water from Subducted Slabs at CMB?

146 It has been considered[1] that the high-temperature stability limit for hydrous phases in the
147 slab at lower-mantle depths is set by the dehydration curve of δ-AlOOH[47], which is close
148 to the normal mantle geotherm (Fig. 1). While $FeOOH_x$ was reported[33] to be stable to
149 3,300 K at 125 GPa, it should be a minor phase in the slab[48,49]. Recent experiments[17,50]
150 showed that $CaCl_2$-type SiO_2, instead of the α-PbO_2-type phase, is stable at CMB
151 conditions in the Al-free SiO_2-H_2O system and contains no water above ~3,600 K.
152 Contrary to these studies suggesting nearly complete dehydration of the slab at the base
153 of the mantle, our experiments demonstrate that Al-bearing SiO_2 in subducted MORB
154 adopts the α-PbO_2-type structure in the lowermost mantle and can possess ~2 wt% H_2O
155 even at 4,100 K (Figs. 3a, b), which corresponds to the temperature for the core side of
156 the CMB (Fig. 1). The pressure of the phase transition between the $CaCl_2$- and α-PbO_2-
157 type structures is found to be similar between dry[19] and hydrous MORB materials.

158 As argued above, the hydrated SiO_2 phase is a main host for water transport by
159 subducting slabs in the shallow to deep lower mantle[2,14,17], unless the crustal layer is
160 delaminated at the 660 km discontinuity[51]. It constitutes 15–30% of MORB crust[19,20] and
161 20–75% of continental crust materials[21,22] and changes crystal structure to α-PbO_2-type
162 in the lowermost mantle (Fig. 1). Once slabs reach the bottom of the mantle, they are
163 heated to 3,400–4,000 K[26–30]. The present experiments demonstrate that Al-bearing α-

164 PbO_2-type SiO_2 in the slab crust does not release water even at such high temperatures as
165 long as it carries H_2O less than ~2 wt% (Figs. 3a, b). Indeed, the amount of H_2O in SiO_2
166 during subduction in the lower mantle is most likely smaller than 2 wt% considering its
167 water storage capacity of ~3.5 to ~1.0 wt% in the shallow to deep lower mantle as recently
168 estimated by Lin & Mao[50]. Even when it is more than 2 wt%, hNT-type SiO_2-AlOOH
169 ss.[46] might form above the CMB and admit water that is not stored in SiO_2. Additional
170 Al_2O_3 necessary to form SiO_2-AlOOH ss. could derive from coexisting bridgmanite/post-
171 perovskite in MORB[18]. Furthermore, an Al- and/or Fe-rich part of the slab crust may
172 include AlOOH-$Mg_{0.5}Si_{0.5}$OOH-FeOOH ss.[1,23–25] as an additional water-bearing phase. It
173 will decompose[1] at least at temperatures along the normal lower-mantle geotherm before
174 arriving at the CMB, and instead SiO_2-AlOOH ss. might be produced.

175 The topmost 2 to 5 km[4,5] in average of the slab mantle is hydrated at the onset of
176 subduction and transports water into the deep mantle. When hydrous phases no longer
177 exist at shallow to middle lower mantle depths[1], bridgmanite and ferropericlase in the
178 uppermost slab mantle become water-saturated[2] (davemaoite will not appear in a depleted
179 peridotite layer). The solubility of water in these nominally anhydrous minerals has been
180 highly controversial but could be as much as ~0.1 wt%[12,13]. When slabs reach the
181 lowermost mantle under high temperatures, the H_2O storage capacity of bridgmanite and

182 ferropericlase will diminish, leading to the exsolution of water from the topmost slab
183 mantle, which turns into hydrous silicate melts. Even so, as soon as such hydrous melts
184 migrate into the neighboring slab crust that is originally 6–7 km thick, all of the H_2O in
185 hydrous melts would redissolve into the SiO_2 phase, fully consuming the silicate melts
186 until SiO_2 becomes saturated with water. Note that both the slab crust and mantle layers
187 have the post-perovskite-dominant lithology in the lowermost mantle[52,53] and are thus
188 easily deformed[54,55]. The stretched and thinned slab mantle layer may be intercalated
189 between the slab crust layers, and the hydrous melts can meet the SiO_2 phase by migrating
190 either upward or downward.

191 Limited Role of Water in the Lowermost Mantle

192 The dehydration of subducted slabs at the base of the mantle has been stressed, and its
193 consequences have been extensively discussed[1,2,34,37,50]. However, our finding of the high
194 capacity of H_2O (~2 wt% in α-PbO_2-type SiO_2 and ~0.3–0.6 wt% in subducted MORB
195 crust) suggests that practically water does not escape from slabs under high temperatures
196 of the CMB region. Therefore, hydration around subducted slabs[1] will not occur and thus
197 not contribute to the formation of low velocity anomalies observed in the LLSVPs[1,31].
198 The ULVZs have often been attributed to the presence of silicate melt above the CMB[35],

199 but the origin of such molten silicate is not likely caused by water. Indeed, the addition
200 of water to MORB does not induce partial melting until α-PbO_2-type SiO_2 becomes H_2O-
201 saturated. It is possible that the CMB temperature is high enough to cause partial melting
202 of subducted crustal materials[40]. Even in this case, water will be largely retained in a solid
203 residue rather than being incorporated into a partial melt; employing D_{H2O} (α-PbO_2-
204 SiO_2/melt) = 2.1 obtained at 128 GPa and 3,850 K close to CMB conditions and the phase
205 proportions found in run #12 (Table 1), we found 73% of H_2O remains in the residue
206 when the degree of partial melting is 31 wt%.

207 The accumulation of water-bearing slabs may have large impacts on viscosity,
208 electrical conductivity, and seismic velocities and attenuation in the lowermost mantle.
209 The incorporation of water largely diminishes the hardness of crystals such as SiO_2
210 quartz[56]. The water-bearing, less viscous slabs might have weaker interactions with
211 LLSVPs, which helps the stability of their structures[57]. The hydrated subducted slabs may
212 cause high electrical conductivity anomalies in the deep lower mantle. The anomalies will
213 be significant when superionic proton motion occurs in Al-bearing hydrous SiO_2, which
214 was found in earlier theoretical simulations[43] under mid-lower mantle *P*-*T* conditions.
215 Seismic velocities of dense dry SiO_2 phases are high compared to those of typical lower-
216 mantle minerals[58]. The incorporation of Al + H in SiO_2 usually decreases the shear and

compressional velocities but increases in the lowermost mantle because of the effect of ferroelastic-type phase transition between stishovite and $CaCl_2$-type phase[59], enhancing high velocity anomalies caused by subducted slabs above the CMB[58].

It has also been proposed[34] that the reaction of water with core metal generates oxygen-rich patches (ORP) at the CMB. They consist mainly of $FeOOH_x$ ($x<1$)[32] formed by superoxidation of iron by water, which exhibits low shear and compressional wave velocities[33] that could account for the ULVZs and exceedingly high electrical conductivity[48,49]. In addition, recent experiments[37] argued the formation of a hydrogen-rich, silicon-deficient layer at the top of the core as a consequence of the reaction between water and Fe-Si core liquid, which can cause low velocity anomalies[36]. However, the water-metal reaction at the CMB should be minimal because practically water does not escape from subducted slabs. The reaction is restricted only at a direct contact between water-bearing SiO_2 crystals and core metal. The hydrated slabs are eventually recycled by being involved in plumes without leaving water in the lowermost mantle. During upwelling, Al-bearing SiO_2 will release water in the shallow lower mantle and the mantle transition zone and finally almost fully dehydrate around 20 GPa where the orthorhombic distortion of the $CaCl_2$-type structure disappears (Figs. 3d, e).

Acknowledgements The authors acknowledge K. Yonemitsu for assisting FIB and EPMA analyses and G. Helffrich for discussion. Comments by W. Panero on an earlier version of the manuscript were helpful. Synchrotron XRD measurements were carried out at BL10XU, SPring-8 (proposals no. 2020A0072, 2020A0066, 2021A0072 and 2021A1481). This work was supported by JSPS Kakenhi to K.H. and H.Y. and by the “Imaging Platform” program by MEXT.

Author contributions The project was designed by K.H. and led by Y.T. SIMS analyses were performed by N.S., H.Y., S.T. and Y.T. XRD data were collected by Y.T. and Y.O. Y.T., K.H. and K.U. wrote the manuscript, and all authors commented on it.

Competing interests The authors declare no competing interests.

Additional information

Correspondence and requests for materials should be addressed to Yutaro Tsutsumi or Kei Hirose.

Table 1 | Chemical compoitions and water concentrations in hydrated SiO_2, SiO_2-AlOOH ss. and melt

Run	#1		#2		#3		#4		#5	
Pressure (GPa)	25 (3)		29 (3)		31 (3)		41 (4)		42 (4)	
Temperature (K)	2900 (150)		3050 (150)		3300 (170)		3000 (150)		2950 (160)	
Duration (sec)	10		4		10		10		6	
Phase	$CaCl_2$-SiO_2	melt	$CaCl_2$-SiO_2	melt	$CaCl_2$-SiO_2	melt	$CaCl_2$-SiO_2	melt	$CaCl_2$-SiO_2	melt
FE-EPMA (wt%)										
SiO_2	87.49 (26)	38.22 (52)	86.74 (47)	41.79 (80)	86.29 (137)	37.95 (67)	87.06 (137)	41.54 (136)	84.26 (278)	38.18 (92)
TiO_2	0.06 (3)	2.43 (10)	0.03 (2)	1.15 (4)	0.06 (2)	1.53 (7)	0.10 (0)	2.21 (28)	0.00 (0)	1.36 (4)
Al_2O_3	8.72 (80)	9.88 (97)	7.37 (55)	7.78 (35)	7.08 (58)	10.19 (8)	8.80 (52)	8.20 (55)	6.82 (94)	8.08 (1)
FeO	0.22 (5)	15.91 (61)	0.16 (10)	15.71 (47)	0.15 (2)	16.98 (51)	0.13 (4)	7.59 (271)	0.25 (0)	22.32 (135)
MgO	0.20 (1)	10.57 (111)	0.17 (8)	7.81 (52)	0.04 (1)	9.85 (4)	0.07 (0)	8.74 (54)	0.10 (7)	7.39 (6)
CaO	0.07 (3)	7.18 (63)	0.14 (9)	6.16 (38)	0.05 (0)	5.33 (18)	0.07 (0)	6.81 (61)	0.13 (9)	5.15 (7)
Na_2O	0.07 (9)	0.40 (7)	0.35 (22)	1.25 (11)	0.11 (9)	0.58 (11)	0.04 (4)	1.16 (51)	0.02 (1)	1.05 (1)
K_2O	0.01 (1)	0.13 (2)	0.01 (1)	0.25 (3)	0.01 (1)	0.12 (1)	0.02 (0)	0.26 (6)	0.00 (0)	0.35 (5)
C	0.50 (65)	1.01 (45)	1.12 (30)	0.74 (17)	1.03 (57)	0.79 (16)	0.71 (38)	0.70 (26)	1.48 (4)	0.45 (6)
SIMS (wt%)										
H_2O	0.51 (2)	1.94 (3)	0.82 (4)	2.60 (6)	0.76 (3)	1.93 (5)	1.27 (5)	2.17 (8)	0.79 (4)	0.99 (5)
Total	97.86	87.66	96.91	85.25	95.57	85.26	98.28	79.39	93.86	85.31

Run	#6		#7		#8		#9		#10	
Pressure (GPa)	42 (4)		50 (5)		51 (5)		58 (6)		59 (6)	
Temperature (K)	3400 (170)		3450 (170)		3350 (170)		3250 (160)		3400 (170)	
Duration (sec)	10		1		30		10		10	
Phase	$CaCl_2$-SiO_2	melt	$CaCl_2$-SiO_2	melt	$CaCl_2$-SiO_2	$CaCl_2$-SiO_2	SiO_2-AlOOH	melt	$CaCl_2$-SiO_2	SiO_2-AlOOH
FE-EPMA (wt%)										
SiO_2	76.48 (265)	28.09 (102)	75.65 (168)	35.48 (26)	86.14 (217)	84.14	60.51 (222)	54.02	87.63 (14)	59.10 (552)
TiO_2	0.06 (6)	2.47 (17)	0.32 (8)	1.69 (9)	0.07 (2)	0.10	0.11 (4)	1.92	0.02 (1)	0.09 (8)
Al_2O_3	11.10 (58)	8.78 (28)	9.60 (19)	13.46 (29)	7.07 (44)	7.63	21.97 (130)	8.61	8.05 (22)	18.12 (267)
FeO	0.51 (16)	15.77 (87)	2.42 (29)	13.22 (31)	0.13 (5)	0.27	0.91 (11)	7.41	0.19 (8)	0.40 (7)
MgO	0.52 (12)	8.43 (7)	2.02 (30)	11.39 (25)	0.06 (0)	0.10	1.69 (28)	7.83	0.10 (3)	1.09 (34)
CaO	0.87 (26)	6.06 (23)	3.04 (18)	6.92 (15)	0.07 (5)	0.11	1.09 (47)	5.87	0.17 (3)	4.82 (163)
Na_2O	0.88 (46)	0.84 (8)	0.49 (6)	1.18 (17)	0.02 (2)	0.17	1.98 (92)	1.39	0.04 (1)	0.25 (7)
K_2O	0.01 (1)	0.21 (1)	0.03 (1)	0.09 (3)	0.01 (1)	0.00	0.06 (4)	0.07	0.01 (1)	0.07 (0)
C	0.87 (12)	1.97 (16)	1.41 (57)	0.90 (18)	0.57 (47)	1.69	1.07 (15)	1.38	1.33 (6)	0.63 (32)
SIMS (wt%)										
H_2O	1.51 (14)	1.73 (7)	1.13 (4)	1.74 (4)	1.18 (4)	1.40 (7)	3.38 (14)	2.13 (8)	1.85 (6)	3.48 (35)
Total	92.81	74.36	96.10	86.07	95.31	95.60	92.78	90.64	99.41	88.05

Run	#11		#12*				#13		#14	
Pressure (GPa)	100 (10)		103 (10)				121 (12)		128 (13)	
Temperature (K)	3500 (180)		3950 (200)				3450 (170)		3850 (190)	
Duration (sec)	5		5				4		4	
Phase	$CaCl_2$-SiO_2	$CaCl_2$-SiO_2	Bdg†	Ca-pv†	melt	$CaCl_2$-SiO_2	melt	α-PbO_2-SiO_2	melt	
FE-EPMA (wt%)										
SiO_2	79.09 (289)	79.29 (214)	46.84 (142)	49.11 (230)	21.73 (97)	78.75 (481)	28.54 (93)	74.61 (230)	22.84 (101)	
TiO_2	0.03 (1)	0.10 (4)	1.15 (8)	0.49 (8)	3.45 (6)	0.04 (3)	3.23 (4)	0.01 (1)	3.69 (15)	
Al_2O_3	13.07 (14)	12.46 (76)	18.23 (38)	2.92 (40)	15.10 (71)	7.60 (46)	17.48 (27)	10.89 (35)	8.20 (48)	
FeO	0.22 (9)	0.33 (17)	5.60 (22)	2.20 (16)	30.05 (85)	0.29 (6)	25.52 (240)	0.09 (3)	27.13 (695)	
MgO	0.42 (34)	2.18 (138)	26.27 (126)	2.52 (49)	12.59 (72)	0.50 (21)	10.50 (29)	0.35 (7)	12.29 (104)	
CaO	0.28 (24)	0.59 (31)	0.81 (17)	34.98 (180)	3.26 (8)	4.91 (237)	3.11 (2)	2.42 (35)	7.21 (105)	
Na_2O	0.10 (6)	0.25 (8)	0.18 (16)	1.72 (31)	0.12 (4)	0.25 (11)	0.18 (4)	0.02 (2)	1.06 (46)	
K_2O	0.01 (1)	0.02 (2)	0.00 (1)	0.36 (4)	0.12 (1)	0.07 (4)	0.09 (2)	0.10 (4)	0.18 (1)	
C	1.29 (10)	1.35 (9)	0.84 (32)	1.17 (46)	1.36 (10)	1.11 (23)	0.90 (22)	0.37 (67)	2.42 (7)	
SIMS (wt%)										
H_2O	2.58 (12)	1.63 (11)			2.14 (10)	3.55 (25)	2.57 (9)	1.94 (9)	0.94 (6)	
Total	97.09	98.19	99.92	95.49	89.94	97.08	92.12	90.79	85.97	

Run	#15		#16		#17		#18	#19	Starting material
Pressure (GPa)	143 (14)		142 (14)		143 (14)		144 (14)	141 (14)	
Temperature (K)	3650 (180)		4100 (210)		4050 (200)		3800 (190)	3850 (190)	
Duration (sec)	4		1		10		1	10	
Phase	α-PbO_2-SiO_2	melt	α-PbO_2-SiO_2	melt	α-PbO_2-SiO_2	melt	α-PbO_2-SiO_2	α-PbO_2-SiO_2	
FE-EPMA (wt%)									
SiO_2	79.81 (126)	28.87 (200)	76.22 (26)	27.07 (62)	81.44 (11)	24.65 (44)	83.82 (99)	70.76 (1)	51.31 (91)
TiO_2	0.02 (3)	3.01 (17)	0.11 (2)	2.89 (10)	0.02 (2)	4.15 (8)	0.08 (3)	0.07 (4)	1.24 (3)
Al_2O_3	10.07 (102)	20.97 (117)	12.56 (8)	17.99 (49)	11.97 (19)	20.49 (20)	11.60 (12)	13.95 (22)	14.90 (61)
FeO	0.15 (2)	21.87 (320)	0.50 (7)	19.40 (32)	0.15 (2)	18.42 (4)	0.71 (7)	0.62 (31)	10.05 (55)
MgO	0.36 (32)	10.98 (57)	0.82 (7)	13.34 (36)	1.92 (10)	15.88 (18)	0.75 (12)	2.32 (20)	8.88 (18)
CaO	1.92 (33)	3.22 (22)	6.13 (24)	3.65 (5)	2.34 (47)	3.46 (14)	2.28 (15)	2.70 (31)	5.37 (12)
Na_2O	0.11 (10)	0.25 (8)	0.36 (4)	1.56 (9)	0.33 (3)	3.15 (12)	0.25 (4)	0.41 (4)	1.74 (8)
K_2O	0.03 (1)	0.14 (1)	-	-	-	-	-	-	0.12 (2)
C	1.29 (11)	1.07 (17)	-	-	-	-	-	-	-
SIMS (wt%)									
H_2O	1.99 (10)	1.84 (14)	1.74 (2)	1.32 (3)	2.17 (3)	1.49 (5)	1.97 (2)	1.84 (2)	2.66 (5)
Total	95.75	92.22	98.45	87.20	100.35	91.68	101.45	92.66	96.27

*Mass balance calculations show 31% melt, 40% SiO_2 phase, 18% Bdg, and 11% Ca-pv by weight.

†Obtained by substracting the composition of coexisting SiO_2 phase by 30.1 and 23.5 wt% for Bdg and Ca-pv, respectively.

Figure Legends

Fig. 1 | Experimental pressure-temperature conditions and lower-mantle geotherms. Present experiments on hydrous MORB found hydrated SiO_2 phases with $CaCl_2$-type (closed circles) and α-PbO_2-type structures (open circles) which coexisted with partial melts at temperatures much higher than normal to hot lower-mantle geotherms (yellow band)[1,60]. Cold geotherm for subducting slabs is given by a blue band[1,2]. Black lines show the solidus and liquidus curves for a dry MORB material[40]. Melts were present even below the anhydrous solidus temperatures because the amount of H_2O added to the sample was more than the capacity of water in solid phases. The green and purple regions indicate the stabilities of phase H (ref. 9) and other hydrous phases[1], respectively, in the slab mantle. The SiO_2 phase in the slab crust is hydrated when they release water mainly at conditions marked by red stars. Recent experiments on hydrated SiO_2 were performed in simple systems; inverted open triangles[16] and pluses[17] in SiO_2-H_2O, closed triangles[18] in SiO_2-Al_2O_3-H_2O. Black broken line shows the dehydration curve of δ-AlOOH (ref. 47). Red line indicates the phase transition boundary in MORB between the $CaCl_2$- and α-PbO_2-type SiO_2 phases[19]. The present experiments demonstrate that α-PbO_2-type SiO_2 can hold ~2 wt% H_2O above melting temperatures of MORB in the CMB region. Pressure and temperature uncertainties are ±10% and ±5%, respectively[61].

Fig. 2 | Cross sections of partially molten samples. Samples were recovered from (**a**) 58 GPa and 3,250 K (run #9) and (**b**) 121 GPa and 3,450 K (run #13). (uppermost panels) EDS X-ray elemental maps combined for Si, Al, Ca and Mg, showing melt, hydrated SiO_2 (red), $CaSiO_3$ perovskite (Ca-pv, blue), SiO_2-AlOOH ss. (Si-Al, light blue), bridgmanite (Bdg, orange) and the dehydrated (sm') and original starting material (sm). (middle panels) Corresponding secondary ion images for $^{28}Si^+$ and $^1H^+$ and the distribution maps of H_2O. These cross sections are slightly different from those for X-ray maps because of repolishing. As a result, the phase boundaries are slightly sifted between them. R. I., relative intensity normalized to that from sm. (lowermost panels) Line profiles of H_2O concentration along the lines A–B and C–D in the middle panels. In **b**, the relatively low water content in an outer melt portion was likely caused by redistribution of water upon the formation of quench crystals during quenching temperature (note that the melt is depleted in SiO_2 and has thus low viscosity). Vertical dashed lines are tie-lines between panels connecting to phase boundaries on the lines A–B and C–D. Scale bars, 10 μm.

Fig. 3 | Variations in hydrated SiO_2. The present experiments on hydrous MORB show data for $CaCl_2$-type (closed circles) and α-PbO_2-type SiO_2 (open circles). Earlier data obtained in water-saturated, SiO_2-H_2O (pluses[17]) and SiO_2-Al_2O_3-H_2O systems (triangles[18]) are also given. Color indicates temperature. **a, b,** Water concentrations in SiO_2 plotted as functions of pressure and temperature, respectively. The water incorporation mechanism (Al + H coupled substitution) for Al-bearing SiO_2 (ref. 18, this study) is different from the interstitial H_2O incorporation into Al-free SiO_2[17], leading to lower solubility at relatively low pressures but higher solubility under deep lower-mantle pressures. **c,** Correlation between Al and H concentrations in SiO_2, indicating the charge-coupled substitution $Si^{4+} = Al^{3+} + H^+$ is a main mechanism for water incorporation (the broken line indicates 1:1 correlation). **d,** The *b*/*a* axial ratio of the $CaCl_2$-type structure observed at 300 K, representing the magnitude of the orthorhombic distortion from the tetragonal structure with *b*/*a* = 1. Present experimental results show the modest effect of H_2O compared to theoretical calculations[43] at 0 K for SiO_2+1.85mol%AlOOH (red, 0.28 wt% H_2O) and SiO_2+6.25mol%AlOOH (blue, 0.94 wt% H_2O). Since the *b*/*a* axial ratios were measured at room temperature, the pressures in **d** are different from those at high temperatures in **a** and **f**. **e,** Correlation between the H_2O content and the *b*/*a* ratio. **f,** SiO_2/melt partition coefficient of H_2O, demonstrating that water is partitioned into SiO_2 more than into silicate melt in the lowermost mantle. The error bars for pressure and temperature are ±10% and ±5%, respectively[61]. Other data are presented as mean values +/- SD (+/- SEM only for the H_2O (H) content from secondary ion image).

1. Ohtani, E. The role of water in Earth's mantle. *Natl. Sci. Rev.* **7**, 224–232 (2020).
2. Walter, M. J. Water transport to the core–mantle boundary. *Natl. Sci. Rev.* **8**, nwab007 (2021).
3. Okamoto, K. & Maruyama, S. The high-pressure synthesis of lawsonite in the MORB + H_2O system. *Am. Mineral.* **84**, 362–373 (1999).
4. van Keken, P. E., Hacker, B. R., Syracuse, E. M. & Abers, G. A. Subduction factory: 4. depth-dependent flux of H_2O from subducting slabs worldwide. *J. Geophys. Res. Solid Earth* **116**, B01401 (2011).
5. Hatakeyama, K., Katayama, I., Hirauchi, K. & Michibayashi, K. Mantle hydration along outer-rise faults inferred from serpentinite permeability. *Sci. Rep.* **7**, 13870 (2017).

6. Tsuchiya, J. First principles prediction of a new high-pressure phase of dense hydrous magnesium silicates in the lower mantle. *Geophys. Res. Lett.* **40**, 4570–4573 (2013).
7. Panero, W. R. & Caracas, R. Stability of phase H in the $MgSiO_4H_2$–AlOOH–SiO_2 system. *Earth Planet. Sci. Lett.* **463**, 171–177 (2017).
8. Nishi, M. *et al.* Stability of hydrous silicate at high pressures and water transport to the deep lower mantle. *Nat. Geosci.* **7**, 224–227 (2014).
9. Ohtani, E., Amaike, Y., Kamada, S., Sakamaki, T. & Hirao, N. Stability of hydrous phase H $MgSiO_4H_2$ under lower mantle conditions. *Geophys. Res. Lett.* **41**, 8283–8287 (2014).
10. Liu, Z. *et al.* Bridgmanite is nearly dry at the top of the lower mantle. *Earth Planet. Sci. Lett.* **570**, 117088 (2021).
11. Bolfan-Casanova, N., Mackwell, S., Keppler, H., McCammon, C. & Rubie, D. C. Pressure dependence of H solubility in magnesiowüstite up to 25 GPa: implications for the storage of water in the Earth's lower mantle. *Geophys. Res. Lett.* **29**, 1449 (2002).
12. Murakami, M., Hirose, K., Yurimoto, H., Nakashima, S. & Takafuji, N. Water in Earth's lower mantle. *Science* **295**, 1885–1887 (2002).
13. Fu, S. *et al.* Water concentration in single-crystal (Al,Fe)-bearing bridgmanite grown from the hydrous melt: implications for dehydration melting at the topmost lower mantle. *Geophys. Res. Lett.* **46**, 10346–10357 (2019).
14. Panero, W. R., Benedetti, L. R. & Jeanloz, R. Transport of water into the lower mantle: role of stishovite. *J. Geophys. Res. Solid Earth* **108**, 2039 (2003).
15. Lin, Y., Hu, Q., Meng, Y., Walter, M. & Mao, H. K. Evidence for the stability of ultrahydrous stishovite in Earth's lower mantle. *Proc. Natl. Acad. Sci. U.S.A.* **117**, 184–189 (2020).
16. Nisr, C. *et al.* Large H_2O solubility in dense silica and its implications for the interiors of water-rich planets. *Proc. Natl. Acad. Sci. U.S.A.* **117**, 9747–9754 (2020).
17. Lin, Y. *et al.* Hydrous SiO_2 in subducted oceanic crust and H_2O transport to the core-mantle boundary. *Earth Planet. Sci. Lett.* **594**, 117708 (2022).
18. Ishii, T. *et al.* Superhydrous aluminous silica phases as major water hosts in high-temperature lower mantle. *Proc. Natl. Acad. Sci. U.S.A.* **119**, e2211243119 (2022).
19. Hirose, K., Takafuji, N., Sata, N. & Ohishi, Y. Phase transition and density of subducted MORB crust in the lower mantle. *Earth Planet. Sci. Lett.* **237**, 239–251 (2005).

20. Ricolleau, A. *et al.* Phase relations and equation of state of a natural MORB: implications for the density profile of subducted oceanic crust in the Earth's lower mantle. *J. Geophys. Res. Solid Earth* **115**, 8202 (2010).
21. Irifune, T., Ringwood, A. E. & Hibberson, W. O. Subduction of continental crust and terrigenous and pelagic sediments: an experimental study. *Earth Planet. Sci. Lett.* **126**, 351–368 (1994).
22. Komabayashi, T., Maruyama, S. & Rino, S. A speculation on the structure of the D" layer: the growth of anti-crust at the core–mantle boundary through the subduction history of the Earth. *Gondwana Res.* **15**, 342–353 (2009).
23. Ohira, I. *et al.* Stability of a hydrous δ-phase, AlOOH–$MgSiO_2(OH)_2$, and a mechanism for water transport into the base of lower mantle. *Earth Planet. Sci. Lett.* **401**, 12–17 (2014).
24. Nishi, M. *et al.* Solid solution and compression behavior of hydroxides in the lower mantle. *J. Geophys. Res. Solid Earth* **124**, 10231–10239 (2019).
25. Walter, M. J. *et al.* The stability of hydrous silicates in Earth's lower mantle: experimental constraints from the systems MgO–SiO_2–H_2O and MgO–Al_2O_3–SiO_2–H_2O. *Chem. Geol.* **418**, 16–29 (2015).
26. Nomura, R. *et al.* Low core-mantle boundary temperature inferred from the solidus of pyrolite. *Science* **343**, 522–525 (2014).
27. Kim, T. *et al.* Low melting temperature of anhydrous mantle materials at the core-mantle boundary. *Geophys. Res. Lett.* **47**, e2020GL089345 (2020).
28. Fiquet, G. *et al.* Melting of peridotite to 140 gigapascals. *Science* **329**, 1516–1518 (2010).
29. Andrault, D. *et al.* Solidus and liquidus profiles of chondritic mantle: implication for melting of the Earth across its history. *Earth Planet. Sci. Lett.* **304**, 251–259 (2011).
30. Deschamps, F. & Cobden, L. Estimating core-mantle boundary temperature from seismic shear velocity and attenuation. *Front. Earth Sci.* **10**, 1031507 (2022).
31. Mashino, I., Murakami, M. & Ohtani, E. Sound velocities of δ-AlOOH up to core-mantle boundary pressures with implications for the seismic anomalies in the deep mantle. *J. Geophys. Res. Solid Earth* **121**, 595–609 (2016).
32. Hu, Q. *et al.* FeO_2 and FeOOH under deep lower-mantle conditions and Earth's oxygen–hydrogen cycles. *Nature* **534**, 241–244 (2016).
33. Liu, J. *et al.* Hydrogen-bearing iron peroxide and the origin of ultralow-velocity zones. *Nature* **551**, 494–497 (2017).
34. Mao, H.-K. *et al.* When water meets iron at Earth's core–mantle boundary. *Natl. Sci. Rev.* **4**, 870–878 (2017).

391 35. Yu, S. & Garnero, E. J. Ultralow velocity zone locations: a global assessment.
392 *Geochem. Geophys. Geosyst.* **19**, 396–414 (2018).
393 36. Helffrich, G. & Kaneshima, S. Outer-core compositional stratification from observed
394 core wave speed profiles. *Nature* **468**, 807–810 (2010).
395 37. Kim, T. *et al.* A hydrogen-enriched layer in the topmost outer core sourced from
396 deeply subducted water. *Nat. Geosci.* **16**, 1208–1214 (2023).
397 38. Ito, E., Kubo, A., Katsura, T. & Walter, M. J. Melting experiments of mantle
398 materials under lower mantle conditions with implications for magma ocean
399 differentiation. *Phys. Earth Planet. Inter.* **143**, 397–406 (2004).
400 39. Tateno, S., Hirose, K. & Ohishi, Y. Melting experiments on peridotite to lowermost
401 mantle conditions. *J. Geophys. Res. Solid Earth* **119**, 4684–4694 (2014).
402 40. Andrault, D. *et al.* Melting of subducted basalt at the core-mantle boundary. *Science*
403 **344**, 892–895 (2014).
404 41. Tateno, S. *et al.* Melting phase relations and element partitioning in MORB to
405 lowermost mantle conditions. *J. Geophys. Res. Solid Earth* **123**, 5515–5531 (2018).
406 42. Lakshtanov, D. L. *et al.* The post-stishovite phase transition in hydrous alumina-
407 bearing SiO_2 in the lower mantle of the earth. *Proc. Natl. Acad. Sci. U.S.A.* **104**,
408 13588–13590 (2007).
409 43. Umemoto, K., Kawamura, K., Hirose, K. & Wentzcovitch, R. M. Post-stishovite
410 transition in hydrous aluminous SiO_2. *Phys. Earth Planet. Inter.* **255**, 18–26 (2016).
411 44. Nomura, R., Hirose, K., Sata, N. & Ohishi, Y. Precise determination of post-
412 stishovite phase transition boundary and implications for seismic heterogeneities in
413 the mid-lower mantle. *Phys. Earth Planet. Inter.* **183**, 104–109 (2010).
414 45. Panero, W. R. & Stixrude, L. P. Hydrogen incorporation in stishovite at high pressure
415 and symmetric hydrogen bonding in δ-AlOOH. *Earth Planet. Sci. Lett.* **221**, 421–
416 431 (2004).
417 46. Liu, L. *et al.* Formation of an Al-rich niccolite-type silica in subducted oceanic crust:
418 implications for water transport to the deep lower mantle. *Geophys. Res. Lett.* **49**,
419 e2021GL097178 (2022).
420 47. Duan, Y. *et al.* Phase stability and thermal equation of state of δ-AlOOH: implication
421 for water transportation to the deep lower mantle. *Earth Planet. Sci. Lett.* **494**, 92–
422 98 (2018).
423 48. Hou, M. *et al.* Superionic iron oxide–hydroxide in Earth's deep mantle. *Nat. Geosci.*
424 **14**, 174–178 (2021).
425 49. Komabayashi, T. Hydrogen dances in the deep mantle. *Nat. Geosci.* **14**, 116–117
426 (2021).

50. Lin, Y. & Mao, H.-K. Dense hydrous silica carrying water to the deep Earth and promotion of oxygen fugacity heterogeneity. *Matter Radiat. Extrem.* **7**, 068101 (2022).
51. Li, M. in *Mantle Convection and Surface Expressions* (eds Marquardt, H. et al.) 303–328 (American Geophysical Union, 2021).
52. Murakami, M., Hirose, K., Sata, N. & Ohishi, Y. Post-perovskite phase transition and mineral chemistry in the pyrolitic lowermost mantle. *Geophys. Res. Lett.* **32**, L03304 (2005).
53. Ohta, K., Hirose, K., Lay, T., Sata, N. & Ohishi, Y. Phase transitions in pyrolite and MORB at lowermost mantle conditions: implications for a MORB-rich pile above the core–mantle boundary. *Earth Planet. Sci. Lett.* **267**, 107–117 (2008).
54. Hunt, S. A. *et al.* Weakening of calcium iridate during its transformation from perovskite to post-perovskite. *Nat. Geosci.* **2**, 794–797 (2009).
55. Ammann, M. W., Brodholt, J. P., Wookey, J. & Dobson, D. P. First-principles constraints on diffusion in lower-mantle minerals and a weak D" layer. *Nature* **465**, 462–465 (2010).
56. Griggs, D. Hydrolytic weakening of quartz and other silicates. *Geophys. J. R. Astr. Soc.* **14**, 19–31 (1967).
57. Li, Y. *et al.* Effects of the compositional viscosity ratio on the long-term evolution of thermochemical reservoirs in the deep mantle. *Geophys. Res. Lett.* **46**, 9591–9601 (2019).
58. Wang, W. *et al.* Velocity and density characteristics of subducted oceanic crust and the origin of lower-mantle heterogeneities. *Nat. Commun.* **11**, 64 (2020).
59. Zhang, Y. *et al.* Elasticity of hydrated Al-bearing stishovite and post-stishovite: Implications for understanding regional seismic V_S anomalies along subducting slabs in the lower mantle. *J. Geophys. Res. Solid Earth* **127**, e2021JB023170 (2022).
60. Brown, J. M. & Shankland, T. J. Thermodynamic parameters in the Earth as determined from seismic profiles. *Geophys. J. Int.* **66**, 579–596 (1981).
61. Tagawa, S. *et al.* Experimental evidence for hydrogen incorporation into Earth's core. *Nat. Commun.* **12**, 2588 (2021).

Methods

Starting material and high pressure-temperature experiments

We used a hydrous glass containing 2.66(5) wt% H_2O as a starting material, which was synthesized at 1.0 GPa and 1,573 K in a piston-cylinder apparatus. Its chemical composition is similar to that of a natural MORB[62], except that the present sample includes water and less than half CaO content (Table 1) such that the SiO_2 phase appears in direct contact with partial melt (Fig. 2). High *P-T* conditions were generated in a laser-heated diamond-anvil cell with flat 300 μm or beveled 120 μm culet diamond anvils. A rhenium gasket was preindented to ~30 μm thick and was drilled a ~40–120 μm hole for a sample chamber. We loaded the hydrous MORB glass sample without pressure medium; nevertheless, sample temperature near the diamond anvils should have been low during laser-heating, and thus the glass sample remained amorphous and acted as a good thermal insulator[28]. The sample was compressed at room temperature and then heated from both sides using a couple of 100 W single-mode Yb fiber lasers at the beamline BL10XU, SPring-8 except for runs #7 and #16–19 in which heating was made at the University of Tokyo with a similar system[63]. The laser spot size was about 30 μm. Temperature was measured by a spectro-radiometric method[64]. Heating duration ranged from 1 to 30 s (typically 10 s). The H_2O contents in SiO_2 and melt and the resulting D_{H2O} found in run #7 with heating for 1 s at 50 GPa and 3,450 K are in good agreement with the results of other runs with longer heating durations at similar *P-T* range (Figs. 3a, f). Furthermore, we obtained similar results in runs #17 and #18 performed at nearly identical *P-T* conditions (~142 GPa and ~4,100 K) with changing heating duration from 1 s to 10 s. These time-series experiments indicate that 1 s is long enough for the attainment of equilibrium water partitioning. Pressure was measured on the basis of the Raman shift of the diamond anvil[65] at 300 K after heating and corrected for thermal pressure contributions[66]. We collected XRD patterns of the sample at high pressures using synchrotron X-rays with an energy of ~30 keV. The lattice parameters and unit-cell volumes of the hydrated SiO_2 phases are shown in Extended Data Table 1 and Extended Data Fig. 3.

Subsequently we released pressure and prepared the sample cross sections for most of the experiments (runs #1–15) at the center of a heated spot parallel to the compression/laser-heating axis by using a focused ion beam (FIB) (*FEI*, Versa 3D DualBeam). We performed textural and compositional characterizations on these cross sections with a field-emission (FE)-type scanning electron microscope (SEM) and an energy dispersive X-ray spectrometry (EDS) (Fig. 2). After SIMS measurements (see

below), the major element compositions except H_2O of coexisting quenched melt and solid phases were determined using an FE-type electron probe micro-analyzer (FE-EPMA) (*JEOL*, JXA-8530F) (Table 1). Analyses were performed with an acceleration voltage of 12 keV and a beam current of 15 nA. We used SiO_2, TiO_2, Al_2O_3, Fe, MgO, $CaSiO_3$, $NaAlSi_3O_8$, $KTiOPO_4$ and Fe_3C as standards and PETJ (Si, Ti, K), TAP (Al, Mg, Na), LIFH (Fe), PETH (Ca) and LDE2H (C) as analyzing crystals. For runs #16–19, the samples were milled by ion beam in a SIMS instrument such that a wider area of SiO_2 was exposed on the surface in a plane normal to the compression/laser-heating axis. We obtained the major element compositions by EDS with a silicon drift detector (*Oxford*, X-Max 150) for these samples, which is attached with an FE-SEM (*JEOL*, JSM-7000F). The EDS measurements were performed with an acceleration voltage of 15 keV and a beam current of 1 nA.

SIMS analyses

Water concentrations in SiO_2, SiO_2-AlOOH ss. and partial melt were obtained by an isotope microscope system, composed of *CAMECA* ims-1270 SIMS equipped with a two-dimensional ion detector, SCAPS (stacked CMOS-type active pixel sensor), at Hokkaido University[61,67–69]. The sample was coated with ~70 nm thick Au layer by plasma sputtering to compensate electrostatic charging on the sample surface. We used $^{16}O^-$ primary beam (13 keV, 37 nA) that was focused to 20–30 μm in diameter and rastered across a 100 μm × 100 μm region on the sample surface. A contrast aperture was set to be 100 μm in diameter. In order to eliminate contributions of adsorbed water on the sample surface[70], we employed the energy slit to be 20 eV and analyzed by -100 V offsetting the sample accelerating voltage. Pressure in a sample chamber during measurements was maintained at about 4.5×10^{-9} Pa. SCAPS images of secondary ions for $^1H^+$, $^{28}Si^+$, $^{27}Al^+$, $^{40}Ca^+$ and $^{24}Mg^+$ were collected after pre-sputtering to obtain stable signals with accumulation time of 300, 50, 25, 50 and 25 s, respectively (Extended Data Fig. 2). Since the SCAPS exhibits a good linear relationship between an output voltage and the number of secondary ions, the abundance of each element can be quantified pixel by pixel from the intensity map. The spatial resolution of quantification is 0.5 μm × 0.5 μm. We employed three silicate glasses with known H_2O concentrations as standards (0.0 to 4.5 wt%)[71] to convert the intensity ratio, $^1H^+/^{28}Si^+$, into the mass ratio. The intensity ratios from secondary ion images and the mass ratios of H/Si of these standards were linearly correlated (correlation coefficient $R^2 = 0.996$)[61]. In order to reduce statistical errors, we applied a moving average method to determine the H/Si mass ratio on each region[68]. Water concentration in each region was then obtained by multiplying the H/Si

ratio by the Si content acquired by major element analyses (Fig. 2). The average water contents for each phase were calculated from the SCAPS image and shown in Table 1.

Data availability

All data supporting this study are available at https://zenodo.org/records/10901809.

62. Hirose, K., Fei, Y., Ma, Y. & Mao, H.-K. The fate of subducted basaltic crust in the Earth's lower mantle. *Nature* **397**, 53–56 (1999).
63. Hasegawa, M., Hirose, K., Oka, K. & Ohishi, Y. Liquidus phase relations and solid-liquid partitioning in the Fe-Si-C system under core pressures. *Geophys. Res. Lett.* **48**, e2021GL092681 (2021).
64. Hirao, N. *et al.* New developments in high-pressure X-ray diffraction beamline for diamond anvil cell at SPring-8. *Matter Radiat. Extrem.* **5**, 018403 (2020).
65. Akahama, Y. & Kawamura, H. High-pressure Raman spectroscopy of diamond anvils to 250GPa: method for pressure determination in the multimegabar pressure range. *J. Appl. Phys.* **96**, 3748–3751 (2004).
66. Hirose, K. *et al.* Crystallization of silicon dioxide and compositional evolution of the Earth's core. *Nature* **543**, 99–102 (2017).
67. Yurimoto, H., Nagashima, K. & Kunihiro, T. High precision isotope micro-imaging of materials. *Appl. Surf. Sci.* **203–204**, 793–797 (2003).
68. Sakamoto, N. *et al.* Remnants of the early solar system water enriched in heavy oxygen isotopes. *Science* **317**, 231–233 (2007).
69. Greenwood, J. P. *et al.* Hydrogen isotope ratios in lunar rocks indicate delivery of cometary water to the Moon. *Nat. Geosci.* **4**, 79–82 (2011).
70. Yurimoto, H., Kurosawa, M. & Sueno, S. Hydrogen analysis in quartz crystals and quartz glasses by secondary ion mass spectrometry. *Geochim. Cosmochim. Acta* **53**, 751–755 (1989).
71. Yoshimura, S. Diffusive fractionation of H_2O and CO_2 during magma degassing. *Chem. Geol.* **411**, 172–181 (2015).
72. Bolfan-Casanova, N., Andrault, D., Amiguet, E. & Guignot, N. Equation of state and post-stishovite transformation of Al-bearing silica up to 100 GPa and 3000 K. *Phys. Earth Planet. Inter.* **174**, 70–77 (2009).
73. Andrault, D. *et al.* Phase diagram and *P-V-T* equation of state of Al-bearing seifertite at lowermost mantle conditions. *Am. Mineral.* **99**, 2035–2042 (2014).

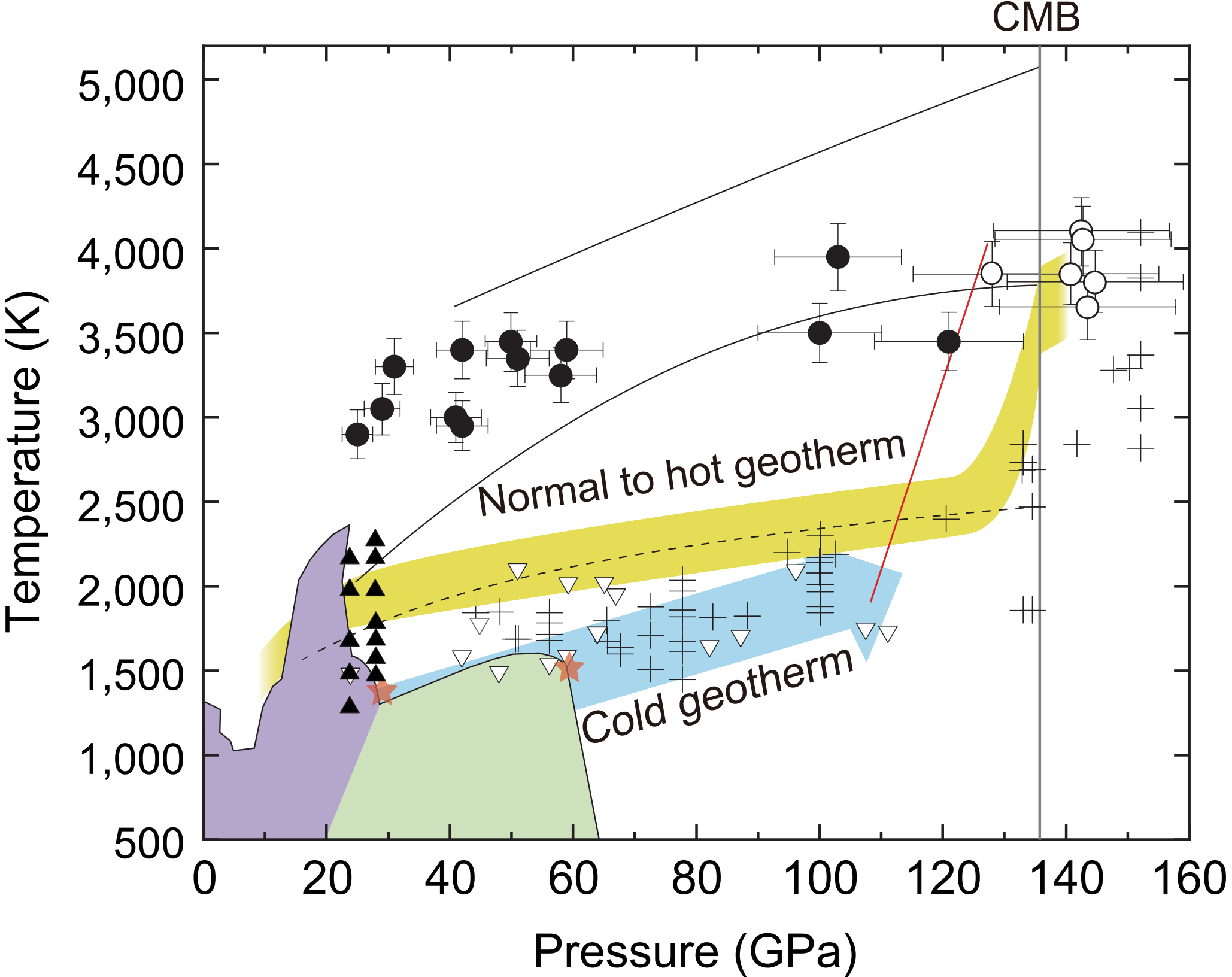
CMB
5,000
4,500
4,000
3,500
3,000
2,500
2,000
1,500
1,000
500
Temperature (K)
0
20
40
60
80
100
120
140
160
Pressure (GPa)
Normal to hot geotherm
Cold geotherm

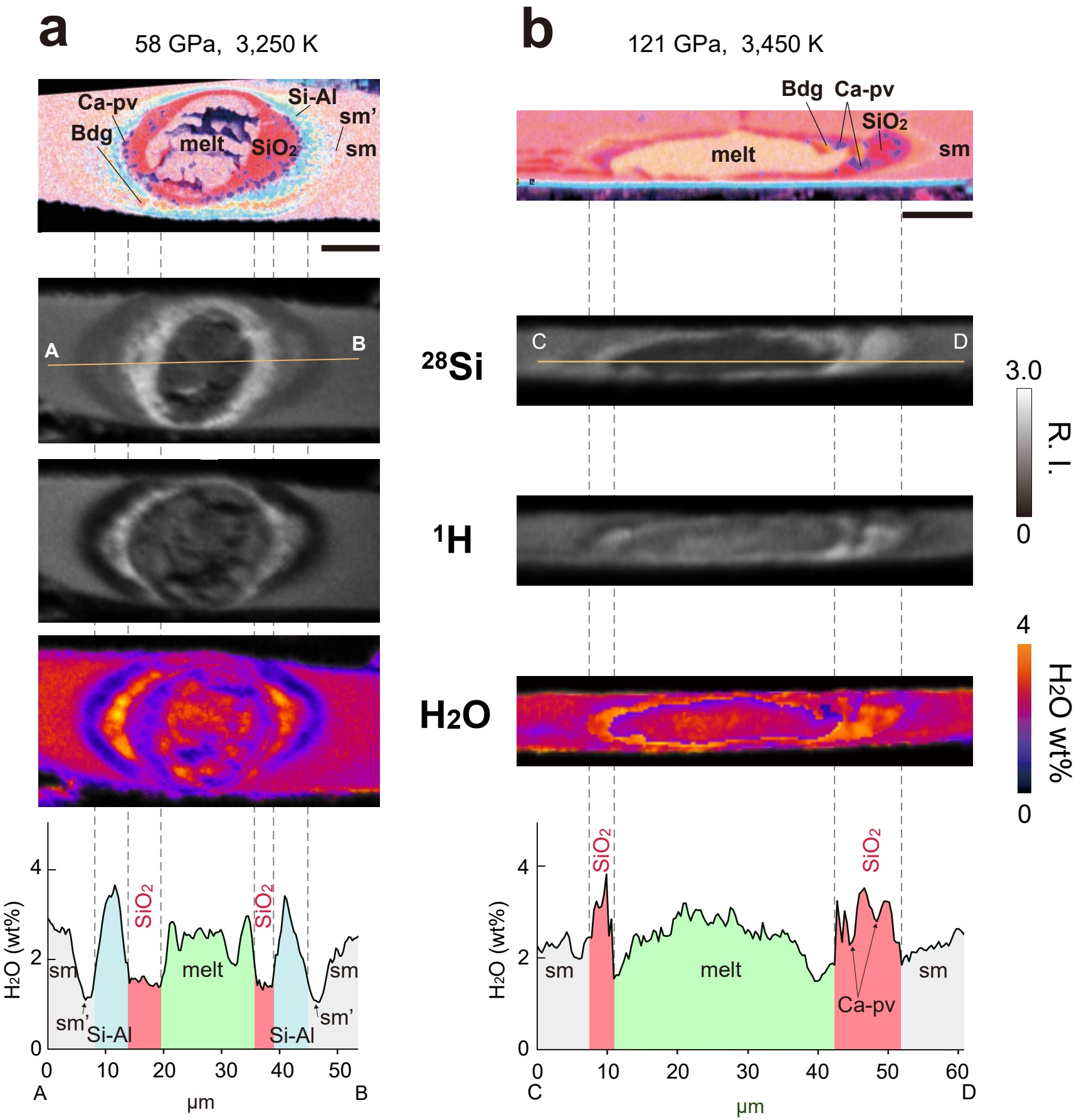
a
58 GPa, 3,250 K
Ca-pv
Bdg
melt
SiO2
Si-Al
sm'
sm
A
B
28Si
1H
H2O
b
121 GPa, 3,450 K
Bdg
Ca-pv
SiO2
melt
sm
C
D
3.0
R. I.
0
4
H2O wt%
0
H2O (wt%)
sm
sm'
Si-Al
SiO2
melt
Ca-pv
μm

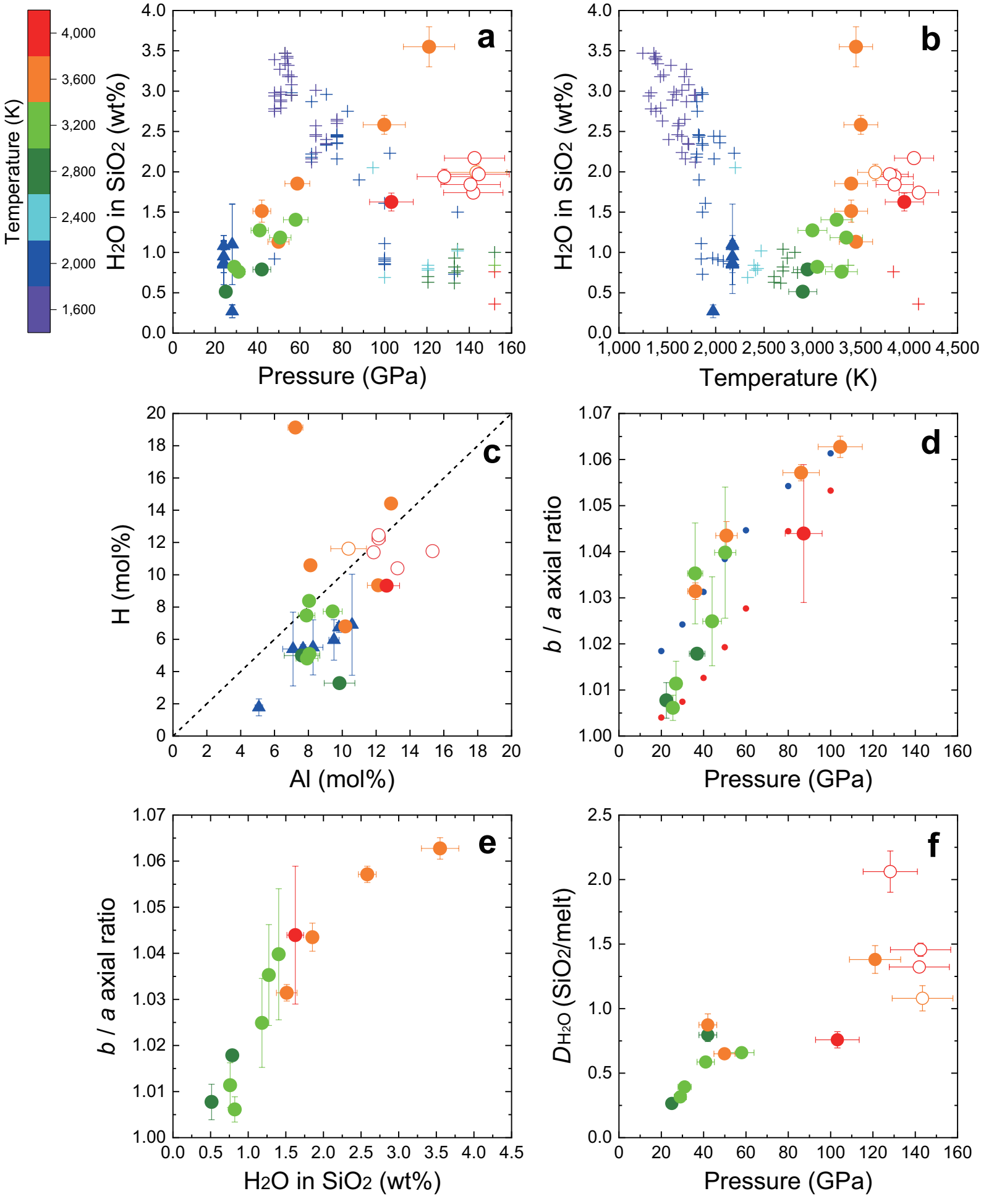
Temperature (K)
4,000
3,600
3,200
2,800
2,400
2,000
1,600
a
H2O in SiO2 (wt%)
Pressure (GPa)
b
H2O in SiO2 (wt%)
Temperature (K)
c
H (mol%)
Al (mol%)
d
b / a axial ratio
Pressure (GPa)
e
b / a axial ratio
H2O in SiO2 (wt%)
f
DH2O (SiO2/melt)
Pressure (GPa)

Table 1 | Chemical compositions and water concentrations in hydrated SiO_2, SiO_2-AlOOH ss. and melt

Run	#1				#2				#3				#4				#5			
Pressure (GPa)	25 (3)				29 (3)				31 (3)				41 (4)				42 (4)			
Temperature (K)	2900 (150)				3050 (150)				3300 (170)				3000 (150)				2950 (160)			
Duration (sec)	10				4				10				10				6			
Phase	$CaCl_2$-SiO_2		melt		$CaCl_2$-SiO_2		melt		$CaCl_2$-SiO_2		melt		$CaCl_2$-SiO_2		melt		$CaCl_2$-SiO_2		melt	
FE-EPMA (wt%)																				
SiO_2	87.49	(26)	38.22	(52)	86.74	(47)	41.79	(80)	86.29	(137)	37.95	(67)	87.06	(137)	41.54	(136)	84.26	(278)	38.18	(92)
TiO_2	0.06	(3)	2.43	(10)	0.03	(2)	1.15	(4)	0.06	(2)	1.53	(7)	0.10	(0)	2.21	(28)	0.00	(0)	1.36	(4)
Al_2O_3	8.72	(80)	9.88	(97)	7.37	(55)	7.78	(35)	7.08	(58)	10.19	(8)	8.80	(52)	8.20	(55)	6.82	(94)	8.08	(1)
FeO	0.22	(5)	15.91	(61)	0.16	(10)	15.71	(47)	0.15	(2)	16.98	(51)	0.13	(4)	7.59	(271)	0.25	(0)	22.32	(135)
MgO	0.20	(1)	10.57	(111)	0.17	(8)	7.81	(52)	0.04	(1)	9.85	(4)	0.07	(0)	8.74	(54)	0.10	(7)	7.39	(6)
CaO	0.07	(3)	7.18	(63)	0.14	(9)	6.16	(38)	0.05	(0)	5.33	(18)	0.07	(0)	6.81	(61)	0.13	(9)	5.15	(7)
Na_2O	0.07	(9)	0.40	(7)	0.35	(22)	1.25	(11)	0.11	(9)	0.58	(11)	0.04	(4)	1.16	(51)	0.02	(1)	1.05	(1)
K_2O	0.01	(1)	0.13	(2)	0.01	(1)	0.25	(3)	0.01	(1)	0.12	(1)	0.02	(0)	0.26	(6)	0.00	(0)	0.35	(5)
C	0.50	(65)	1.01	(45)	1.12	(30)	0.74	(17)	1.03	(57)	0.79	(16)	0.71	(38)	0.70	(26)	1.48	(4)	0.45	(6)
SIMS (wt%)																				
H_2O	0.51	(2)	1.94	(3)	0.82	(4)	2.60	(6)	0.76	(3)	1.93	(5)	1.27	(5)	2.17	(8)	0.79	(4)	0.99	(5)
Total	97.86		87.66		96.91		85.25		95.57		85.26		98.28		79.39		93.86		85.31	

Run	#6				#7				#8				#9						#10			
Pressure (GPa)	42 (4)				50 (5)				51 (5)				58 (6)						59 (6)			
Temperature (K)	3400 (170)				3450 (170)				3350 (170)				3250 (160)						3400 (170)			
Duration (sec)	10				1				30				10						10			
Phase	$CaCl_2$-SiO_2		melt		$CaCl_2$-SiO_2		melt		$CaCl_2$-SiO_2		$CaCl_2$-SiO_2		SiO_2-AlOOH		melt				$CaCl_2$-SiO_2		SiO_2-AlOOH	
FE-EPMA (wt%)																						
SiO_2	76.48	(265)	28.09	(102)	75.65	(168)	35.48	(26)	86.14	(217)	84.14		60.51	(222)	54.02				87.63	(14)	59.10	(552)
TiO_2	0.06	(6)	2.47	(17)	0.32	(8)	1.69	(9)	0.07	(2)	0.10		0.11	(4)	1.92				0.02	(1)	0.09	(8)
Al_2O_3	11.10	(58)	8.78	(28)	9.60	(19)	13.46	(29)	7.07	(44)	7.63		21.97	(130)	8.61				8.05	(22)	18.12	(267)
FeO	0.51	(16)	15.77	(87)	2.42	(29)	13.22	(31)	0.13	(5)	0.27		0.91	(11)	7.41				0.19	(8)	0.40	(7)
MgO	0.52	(12)	8.43	(7)	2.02	(30)	11.39	(25)	0.06	(0)	0.10		1.69	(28)	7.83				0.10	(3)	1.09	(34)
CaO	0.87	(26)	6.06	(23)	3.04	(18)	6.92	(15)	0.07	(5)	0.11		1.09	(47)	5.87				0.17	(3)	4.82	(163)
Na_2O	0.88	(46)	0.84	(8)	0.49	(6)	1.18	(17)	0.02	(2)	0.17		1.98	(92)	1.39				0.04	(1)	0.25	(7)
K_2O	0.01	(1)	0.21	(1)	0.03	(1)	0.09	(3)	0.01	(1)	0.00		0.06	(4)	0.07				0.01	(1)	0.07	(0)
C	0.87	(12)	1.97	(16)	1.41	(57)	0.90	(18)	0.57	(47)	1.69		1.07	(15)	1.38				1.33	(6)	0.63	(32)
SIMS (wt%)																						
H_2O	1.51	(14)	1.73	(7)	1.13	(4)	1.74	(4)	1.18	(4)	1.40	(7)	3.38	(14)	2.13	(8)			1.85	(6)	3.48	(35)
Total	92.81		74.36		96.10		86.07		95.31		95.60		92.78		90.64				99.41		88.05	

Run	#11				#12*								#13				#14					
Pressure (GPa)	100 (10)				103 (10)								121 (12)				128 (13)					
Temperature (K)	3500 (180)				3950 (200)								3450 (170)				3850 (190)					
Duration (sec)	5				5								4				4					
Phase	$CaCl_2$-SiO_2				$CaCl_2$-SiO_2		Bdg†		Ca-pv†		melt		$CaCl_2$-SiO_2		melt		α-PbO_2-SiO_2		melt			
FE-EPMA (wt%)																						
SiO_2	79.09	(289)			79.29	(214)	46.84	(142)	49.11	(230)	21.73	(97)	78.75	(481)	28.54	(93)	74.61	(230)	22.84	(101)		
TiO_2	0.03	(1)			0.10	(4)	1.15	(8)	0.49	(8)	3.45	(6)	0.04	(3)	3.23	(4)	0.01	(1)	3.69	(15)		
Al_2O_3	13.07	(14)			12.46	(76)	18.23	(38)	2.92	(40)	15.10	(71)	7.60	(46)	17.48	(27)	10.89	(35)	8.20	(48)		
FeO	0.22	(9)			0.33	(17)	5.60	(22)	2.20	(16)	30.05	(85)	0.29	(6)	25.52	(240)	0.09	(3)	27.13	(695)		
MgO	0.42	(34)			2.18	(138)	26.27	(126)	2.52	(49)	12.59	(72)	0.50	(21)	10.50	(29)	0.35	(7)	12.29	(104)		
CaO	0.28	(24)			0.59	(31)	0.81	(17)	34.98	(180)	3.26	(8)	4.91	(237)	3.11	(2)	2.42	(35)	7.21	(105)		
Na_2O	0.10	(6)			0.25	(8)	0.18	(16)	1.72	(31)	0.12	(4)	0.25	(11)	0.18	(4)	0.02	(2)	1.06	(46)		
K_2O	0.01	(1)			0.02	(2)	0.00	(1)	0.36	(4)	0.12	(1)	0.07	(4)	0.09	(2)	0.10	(4)	0.18	(1)		
C	1.29	(10)			1.35	(9)	0.84	(32)	1.17	(46)	1.36	(10)	1.11	(23)	0.90	(22)	0.37	(67)	2.42	(7)		
SIMS (wt%)																						
H_2O	2.58	(12)			1.63	(11)					2.14	(10)	3.55	(25)	2.57	(9)	1.94	(9)	0.94	(6)		
Total	97.09				98.19		99.92		95.49		89.94		97.08		92.12		90.79		85.97			

Run	#15				#16				#17				#18				#19				Starting material	
Pressure (GPa)	143 (14)				142 (14)				143 (14)				144 (14)				141 (14)					
Temperature (K)	3650 (180)				4100 (210)				4050 (200)				3800 (190)				3850 (190)					
Duration (sec)	4				1				10				1				10					
Phase	α-PbO_2-SiO_2		melt		α-PbO_2-SiO_2		melt		α-PbO_2-SiO_2		melt		α-PbO_2-SiO_2				α-PbO_2-SiO_2					
FE-EPMA (wt%)																						
SiO_2	79.81	(126)	28.87	(200)	76.22	(26)	27.07	(62)	81.44	(11)	24.65	(44)	83.82	(99)			70.76	(1)			51.31	(91)
TiO_2	0.02	(3)	3.01	(17)	0.11	(2)	2.89	(10)	0.02	(2)	4.15	(8)	0.08	(3)			0.07	(4)			1.24	(3)
Al_2O_3	10.07	(102)	20.97	(117)	12.56	(8)	17.99	(49)	11.97	(19)	20.49	(20)	11.60	(12)			13.95	(22)			14.90	(61)
FeO	0.15	(2)	21.87	(320)	0.50	(7)	19.40	(32)	0.15	(2)	18.42	(4)	0.71	(7)			0.62	(31)			10.05	(55)
MgO	0.36	(32)	10.98	(57)	0.82	(7)	13.34	(36)	1.92	(10)	15.88	(18)	0.75	(12)			2.32	(20)			8.88	(18)
CaO	1.92	(33)	3.22	(22)	6.13	(24)	3.65	(5)	2.34	(47)	3.46	(14)	2.28	(15)			2.70	(31)			5.37	(12)
Na_2O	0.11	(10)	0.25	(8)	0.36	(4)	1.56	(9)	0.33	(3)	3.15	(12)	0.25	(4)			0.41	(4)			1.74	(8)
K_2O	0.03	(1)	0.14	(1)	-		-		-		-		-				-				0.12	(2)
C	1.29	(11)	1.07	(17)	-		-		-		-		-				-				-	
SIMS (wt%)																						
H_2O	1.99	(10)	1.84	(14)	1.74	(2)	1.32	(3)	2.17	(3)	1.49	(5)	1.97	(2)			1.84	(2)			2.66	(5)
Total	95.75		92.22		98.45		87.20		100.35		91.68		101.45				92.66				96.27	

*Mass balance calculations show 31% melt, 40% SiO_2 phase, 18% Bdg, and 11% Ca-pv by weight.
†Obtained by subtracting the composition of coexisting SiO_2 phase by 30.1 and 23.5 wt% for Bdg and Ca-pv, respectively.

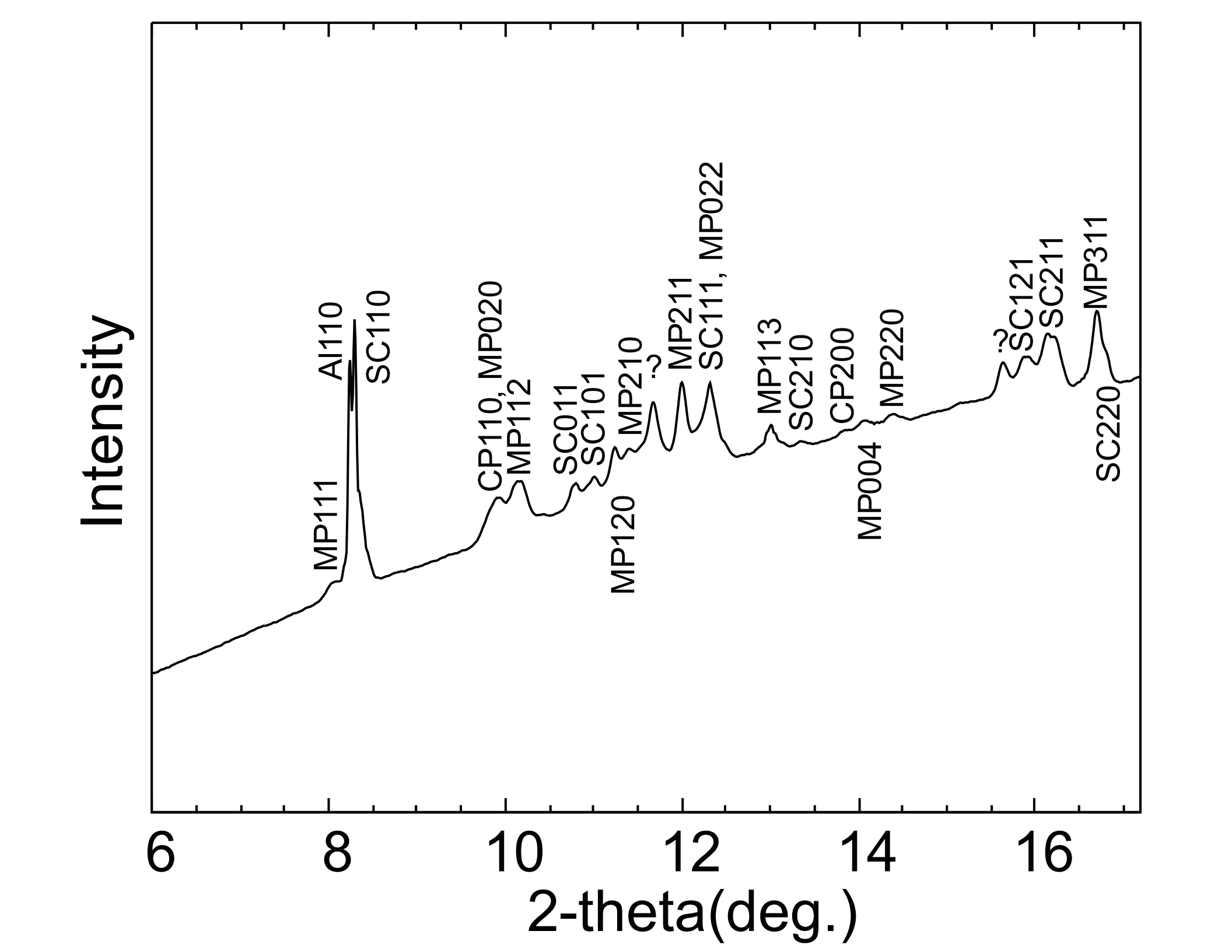
Intensity
6
8
10
12
14
16
2-theta(deg.)
MP111
Al110
SC110
CP110, MP020
MP112
SC011
SC101
MP120
MP210
?
MP211
SC111, MP022
MP113
SC210
CP200
MP004
MP220
?
SC121
SC211
MP311
SC220

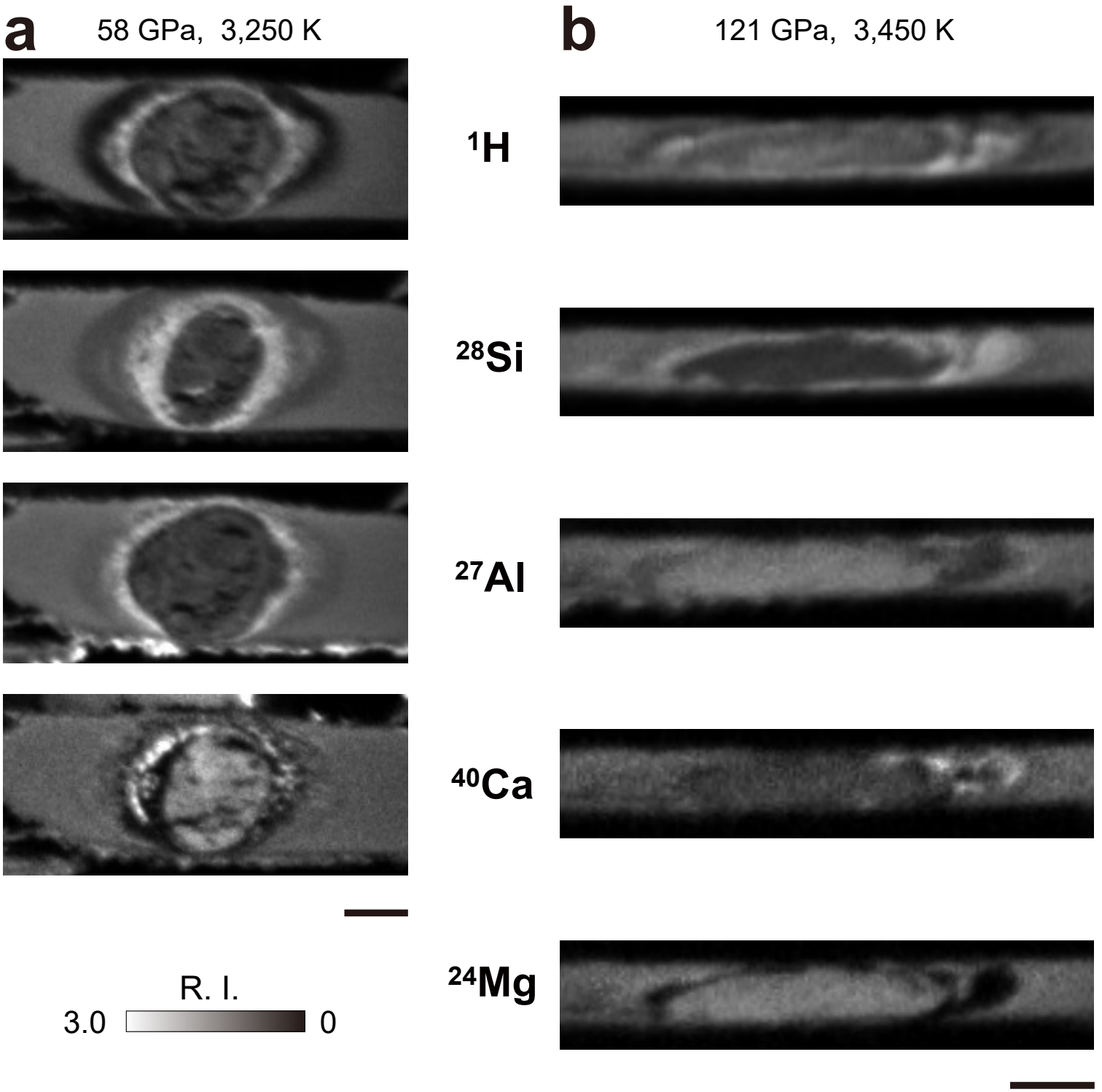
a
58 GPa, 3,250 K
b
121 GPa, 3,450 K
^{1}H
^{28}Si
^{27}Al
^{40}Ca
^{24}Mg
R. I.
3.0
0

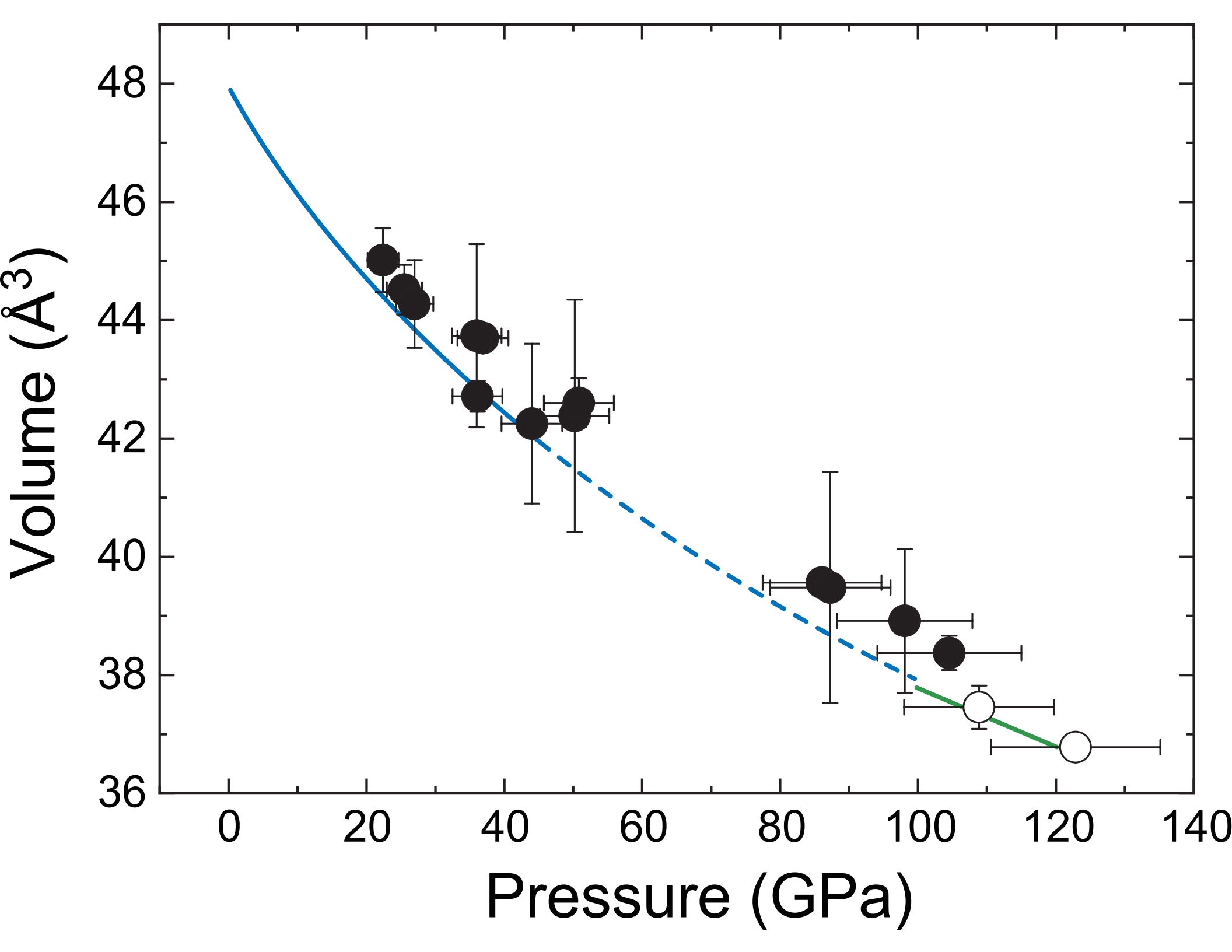
Volume (Å^3)
48
46
44
42
40
38
36
0
20
40
60
80
100
120
140
Pressure (GPa)

Extended Data Table 1 | Lattice constants and unit-cell volumes of the SiO_2 phases

Run	Pressure (GPa)	*a* (Å)	*b* (Å)	*c* (Å)	Volume (Å^3)
$CaCl_2$-type phase					
#1	22 (2)	4.088 (12)	4.120 (11)	2.673 (4)	45.02 (54)
#2	26 (3)	4.076 (6)	4.101 (10)	2.663 (5)	44.52 (42)
#3	27 (3)	4.056 (14)	4.102 (14)	2.661 (9)	44.28 (74)
#4	36 (4)	3.996 (29)	4.137 (32)	2.646 (16)	43.74 (155)
#5	37 (4)	4.027 (1)	4.098 (1)	2.648 (1)	43.70 (8)
#6	36 (4)	3.959 (3)	4.084 (6)	2.642 (3)	42.71 (26)
#8	44 (4)	3.959 (26)	4.057 (28)	2.631 (14)	42.25 (135)
#9	50 (5)	3.940 (37)	4.097 (41)	2.625 (20)	42.38 (197)
#10	51 (5)	3.948 (7)	4.120 (9)	2.619 (4)	42.60 (42)
#11	86 (9)	3.834 (4)	4.053 (5)	2.546 (2)	39.56 (23)
#12	87 (9)	3.870 (38)	4.040 (42)	2.525 (20)	39.48 (195)
#13	105 (11)	3.784 (5)	4.022 (7)	2.522 (3)	38.38 (29)
α-PbO_2-type phase					
#14	109 (11)	3.781 (7)	4.709 (15)	4.208 (7)	74.91 (73)
#15	123 (12)	3.751 (3)	4.694 (2)	4.178 (1)	73.56 (15)

All data were collected at room temperature.